communications biology

Article

https://doi.org/10.1038/s42003-024-07072-x

Decoding the multiple functions of ZBP1 in the mechanism of sepsis-induced acute lung injury

Ting Gong [1,2,7] ✉, Yu Fu [1,3,7], Qingde Wang [1], Patricia A. Loughran[1], Yuehua Li[1], Timothy R. Billiar [1,4], Zongmei Wen[3], Youtan Liu[2] & Jie Fan [1,4,5,6] ✉

Sepsis-induced acute lung injury (ALI), characterized by severe hypoxemia and pulmonary leakage, remains a leading cause of mortality in intensive care units. The exacerbation of ALI during sepsis is largely attributed to uncontrolled inflammatory responses and endothelial dysfunction. Emerging evidence suggests an important role of Z-DNA binding protein 1 (ZBP1) as a sensor in innate immune to drive inflammatory signaling and cell death during infections. However, the role of ZBP1 in sepsis-induced ALI has yet to be defined. We utilized ZBP1 knockout mice and combined single-cell RNA sequencing with experimental validation to investigate ZBP1's roles in the regulation of macrophages and lung endothelial cells during sepsis. We demonstrate that in sepsis, ZBP1 deficiency in macrophages reduces mitochondrial damage and inhibits glycolysis, thereby altering the metabolic status of macrophages. Consequently, this metabolic shift leads to a reduction in the differentiation of macrophages into pro-inflammatory states and decreases macrophage pyroptosis triggered by activation of the NLRP3 inflammasome. These changes significantly weaken the inflammatory signaling pathways between macrophages and endothelial cells and alleviate endothelial dysfunction and cellular damage. These findings reveal important roles for ZBP1 in mediating multiple pathological processes involved in sepsis-induced ALI by modulating the functional states of macrophages and endothelial cells, thereby highlighting its potential as a promising therapeutic target.

Acute Lung Injury (ALI) and acute respiratory distress syndrome (ARDS) are clinical syndromes characterized by severe hypoxemia and pulmonary leakage, posing not only a threat to patient life but also imposing significant psychological and economic burdens on patients and their families[1]. Despite medical advancements over the past few decades, such as implementing low tidal volume ventilation strategies to minimize ventilator-associated lung injury and the use of anti-inflammatory medications like dexamethasone, these interventions have not significantly improved patient survival rates[2,3]. Currently, the mortality rates for ALI/ARDS remain alarmingly high, ranging from 30% to 40%, and account for approximately 10% of all deaths in intensive care units (ICUs) globally[4].

Sepsis is a leading cause of ALI/ARDS, characterized by an uncontrolled inflammatory response and endothelial barrier dysfunction[5]. During sepsis, the extensive release of inflammatory mediators precipitates a systemic inflammatory response syndrome (SIRS), which subsequently triggers ALI/ARDS[6]. In septic ALI, the dysfunction of pulmonary vascular endothelial cells (PVECs) is characterized by increased vascular permeability and the disruption of the alveolar-capillary barrier. This disruption leads to pulmonary edema and compromised gas exchange, resulting in life-threatening hypoxemia and respiratory failure[7]. Therefore, the development of innovative therapeutic strategies targeting septic ALI is critical. Such strategies should focus on controlling the inflammatory response and preserving endothelial barrier function to reduce mortality rates.

Single-cell RNA sequencing (scRNA-seq) is a cutting-edge technology that allows us to decode cellular heterogeneity, differentiation, and intercellular communication during the pathogenesis of sepsis. Evidence indicates that many genes expressed in macrophages and endothelial cells (ECs) are clustered, enabling the identification of gene transcription and

[1]Department of Surgery, University of Pittsburgh School of Medicine, Pittsburgh, 15213, USA. [2]Department of Anesthesiology, Shenzhen Hospital, Southern Medical University, Shenzhen, 518000, China. [3]Department of Anesthesiology, Shanghai Pulmonary Hospital, School of Medicine, Tongji University, Shanghai, 200433, China. [4]Department of Immunology, University of Pittsburgh School of Medicine, Pittsburgh, 15213, USA. [5]Research and Development, Veterans Affairs Pittsburgh Healthcare System, Pittsburgh, PA, 15240, USA. [6]McGowan Institute for Regenerative Medicine, University of Pittsburgh, Pittsburgh, PA, 15219, USA. [7]These authors contributed equally: Ting Gong, Yu Fu. ✉e-mail: tinggong@pitt.edu; jif7@pitt.edu

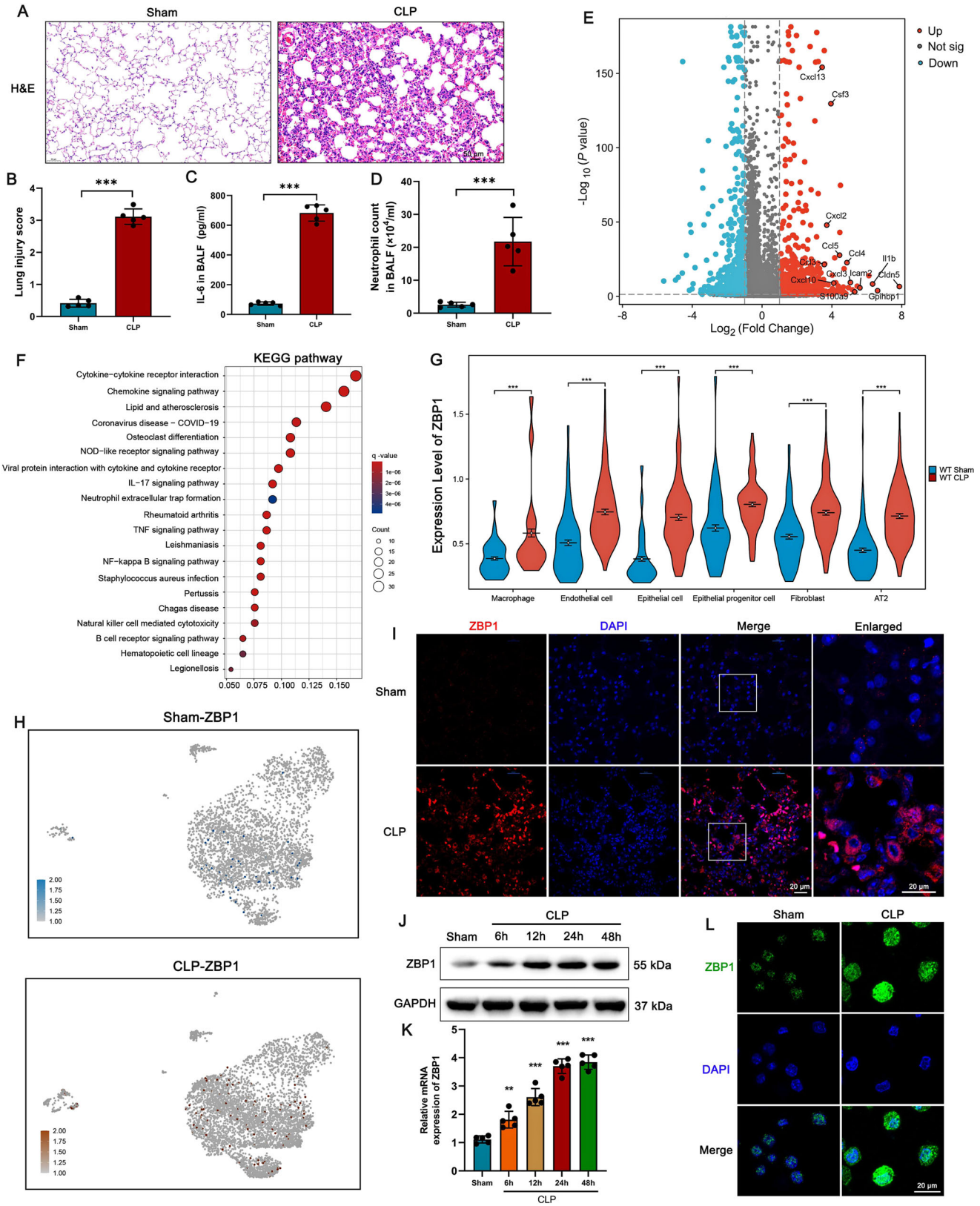

pathological changes in local tissues during the progression of sepsis[8,9]. In this study, we applied scRNA-seq to decode the roles of Z-DNA binding protein 1 (ZBP1) in the mechanism of sepsis-induced ALI.

ZBP1 has been reported as a sensor of double-stranded DNA and RNA helices, adopting the unusual left-handed Z-conformations known as Z-DNA and Z-RNA[10]. Recent studies have identified ZBP1 as a crucial upstream regulator in the pathways of cell death and pro-inflammatory signaling[11,12]. However, the precise role and underlying mechanisms of ZBP1 in the context of sepsis-induced ALI remain poorly understood. In this study, we used ZBP1 knockout ($Zbp1^{-/-}$) mice to investigate the role of

Fig. 1 | ZBP1 expression increases in lung cells in response to sepsis. **A** Representative H&E-stained images of mouse lung tissues 24 h after CLP and sham procedures. Scale bars, 50 μm. **B** Lung injury was quantitatively assessed through the scoring of histopathological features. **C** ELISA detection of IL-6 levels in BALF from CLP mice. **D** Neutrophil exudation counts in BALF. **E** Differential gene expression between WT CLP and WT Sham groups is presented in a volcano plot. Genes upregulated in the WT CLP group are shown as red dots, while downregulated genes are shown as blue dots. **F** Enrichment analysis of upregulated genes in the WT CLP group identified significant KEGG pathways, with the *y*-axis representing pathway items and the *x*-axis displaying the enrichment score. **G** Violin plots from single-cell analysis display the expression levels of ZBP1 mRNA in different cell types between the two groups. **H** UMAP plots represent the distribution of ZBP1 mRNA expression across all analyzed cells, with color intensity corresponding to expression level. **I** Immunofluorescence detection of ZBP1 expression in lung tissue 24 h post-CLP. **J** Western blot and qPCR (**K**) analysis were used to examine ZBP1 protein and mRNA expression levels in lung tissue at 6, 12, 24, and 48 h post-CLP surgery. **L** Localization and expression of ZBP1(green) in macrophages from BALF of septic mice detected by IF. Scale bar, 20 μm. All results are based on three replicates, and data are presented as the mean ± SD, $^{*}P < 0.05$, $^{**}P < 0.01$, $^{***}P < 0.001$.

ZBP1 in sepsis-induced ALI. Utilizing a combination of scRNA-seq, immunofluorescence, and protein blot analysis, we observed an upregulation of ZBP1 expression across various cellular components of the lung during the pathological process of sepsis-induced ALI. Our comprehensive analysis of scRNA-seq data delineates the role of ZBP1 in the progression of sepsis-induced ALI, demonstrating its regulatory influence on various pulmonary cellular components, including macrophages and endothelial cells. The absence of ZBP1 provides a protective effect against lung tissue damage in sepsis-induced ALI, primarily manifesting as reduced inflammatory responses and preserved vascular integrity. These findings highlight ZBP1 as a potential therapeutic target for sepsis-induced ALI and underscore the need for further investigation into its regulatory mechanisms and therapeutic implications.

Results

scRNA-seq reveals alterations in different lung cells following sepsis

A comprehensive illustration outlines the experimental workflow beginning with the induction of the cecal ligation and puncture (CLP) sepsis model in mice. The measurement process includes lung tissue extraction, isolation of single cells, and their analysis through next-generation sequencing using the 10x Genomics platform, followed by detailed bioinformatic analysis and subsequent validation of the findings (Supplementary Fig. 1A).

We utilized UMAP to identify cell clusters based on the expression of a panel of known cell type-specific marker genes. Through this bioinformatic approach, we were able to delineate ten major somatic cell types present in the lung tissue of wild-type mice subjected to either sham (WT Sham) or CLP (WT CLP). These identified cell populations included epithelial cells, mononuclear phagocytes (MPC), endothelial cells, alveolar type 2 cells (AT2), epithelial progenitor cells, fibroblasts, mesothelial cells, macrophages, pericytes, and lymphatic endothelial cells. The UMAP plots display distinct cellular groupings in both WT Sham and WT CLP groups, demonstrating the diversity of cell types and the impact of septic injury on the lung cellular microenvironment. Dot plot analysis further confirmed the presence and relative expression levels of key markers within these cell types, providing a comprehensive cellular atlas of the septic lungs (Supplementary Fig. 1B, C).

In the intercellular interaction network diagrams, we observed connections and changes in the interactions among single-cell subpopulations in the lungs of septic mice (Supplementary Fig. 1D, E). Furthermore, the analysis of enriched signaling pathways reveals significant upregulation of pro-inflammatory pathways, including TNF, IL6, and IL1, in CLP mice. Conversely, in sham mice, pathways such as WNT and VEGF are notably enhanced (Supplementary Fig. 1F).

To further analyze the changes in intercellular interaction pathways during sepsis, we examined the probabilities of macrophage receptor-ligand pairs. We observed a significant enhancement in both paracrine (macrophages affecting other cells) and autocrine (macrophages affecting themselves) pathways in sepsis. This was notably marked by the secretion of TNF and its binding to receptors such as Tnf - Tnfrsf1b, Tnf - Tnfrsf1a, and Spp1 - (Itga4+Itgb1) (Supplementary Fig. 2A–D). Subsequently, we conducted a detailed analysis of macrophage subgroups through dimensionality reduction, clustering, and subgrouping of macrophages (Supplementary Fig. 2E).

scMetabolism software[13] was utilized to assess the activity of the glycolysis pathway in macrophages, with AUCell[14] employed for scoring. We observed a significant enhancement of glycolysis/gluconeogenesis metabolism in macrophages of CLP mice (Supplementary Fig. 3A, B). Furthermore, we found that glycolysis-related genes HIF1-alpha, LDHA, and Slc2a1 were significantly upregulated in the CLP group (Supplementary Fig. 3C–E). Additionally, the inflammatory response and hypoxia pathway activity scores were markedly higher in CLP mice compared to sham mice (Supplementary Fig. 3F–I). Moreover, by referring to the functional gene sets for macrophages summarized by Bischoff[15], the analysis of M1 and M2 pathway activation scores revealed that the M1 macrophage scores were significantly elevated in the CLP mice (Supplementary Fig. 3J).

These results suggest that in sepsis, macrophages predominantly engage in hypoxia and glycolysis pathways, undergo metabolic reprogramming towards a pro-inflammatory M1 polarization, and release inflammatory mediators that affect the function of other cell types.

ZBP1 expression increases in lung cells in response to sepsis

Lung histology demonstrated cellular infiltration, edema, and alveolar wall thickening in the CLP group (Fig. 1A). The severity of lung injury in the CLP group was further quantified with scoring of these histopathological features (Fig. 1B). The bronchoalveolar lavage fluid (BALF) from the CLP group exhibited a marked increase in IL-6 levels (Fig. 1C) and neutrophil exudation (Fig. 1D).

Differences in gene expression between WT CLP and WT Sham groups were delineated in a volcano plot, using a cutoff of $|\log_2 FC| = 1$ and $P = 0.05$. Genes surpassing this threshold of $\log_2 FC > 1$ and $P < 0.05$ were classified as upregulated in the WT CLP group. Among these, the expressions of key inflammatory and chemotactic factors, such as Cxcl2, Ccl5, Ccl4, Il1b, and Cxcl10, were notably elevated in the WT CLP group, suggesting active inflammatory signaling (Fig. 1E). To further probe into the biological significance of these differentially regulated genes, pathway enrichment analysis was conducted. This analysis brought to light a significant enrichment within the cytokine-receptor interaction and the TNF signaling pathway (Fig. 1F), elucidating the molecular mechanisms at play during ALI.

Moreover, the distribution and expression levels of ZBP1 mRNA across different cell populations were elucidated, revealing a marked increase in the CLP group (Fig. 1G). This elevation was visually captured and quantified through UMAP analysis, depicting widespread upregulation of ZBP1 mRNA expression (Fig. 1H). Immunofluorescence staining corroborated these findings, showing pronounced expression of ZBP1 in the lung tissue cells of CLP mice, thus aligning with the transcriptional data (Fig. 1I). Further analyses using Western blot and qPCR to examine ZBP1 protein levels and mRNA revealed significant increase in ZBP1 post-CLP, peaking at the 24 h postoperative interval (Fig. 1J, K).

The increased expression of ZBP1 in macrophages was further validated in the macrophages isolated from the BALF of septic mice. While ZBP1 was primarily in nuclear and minimally expressed in the macrophages from sham group, it exhibited a substantial cytoplasmic presence with significantly elevated expression levels in the macrophages from CLP group (Fig. 1L). The data reveal significant changes in ZBP1 expression and intracellular translocation in the lung following sepsis-induced ALI.

ZBP1 is involved in sepsis-induced lung injury and mortality

The pivotal role of ZBP1 in sepsis-induced ALI was shown through a comparative analysis of *Zbp1*$^{-/-}$ and WT mice following CLP. Lung

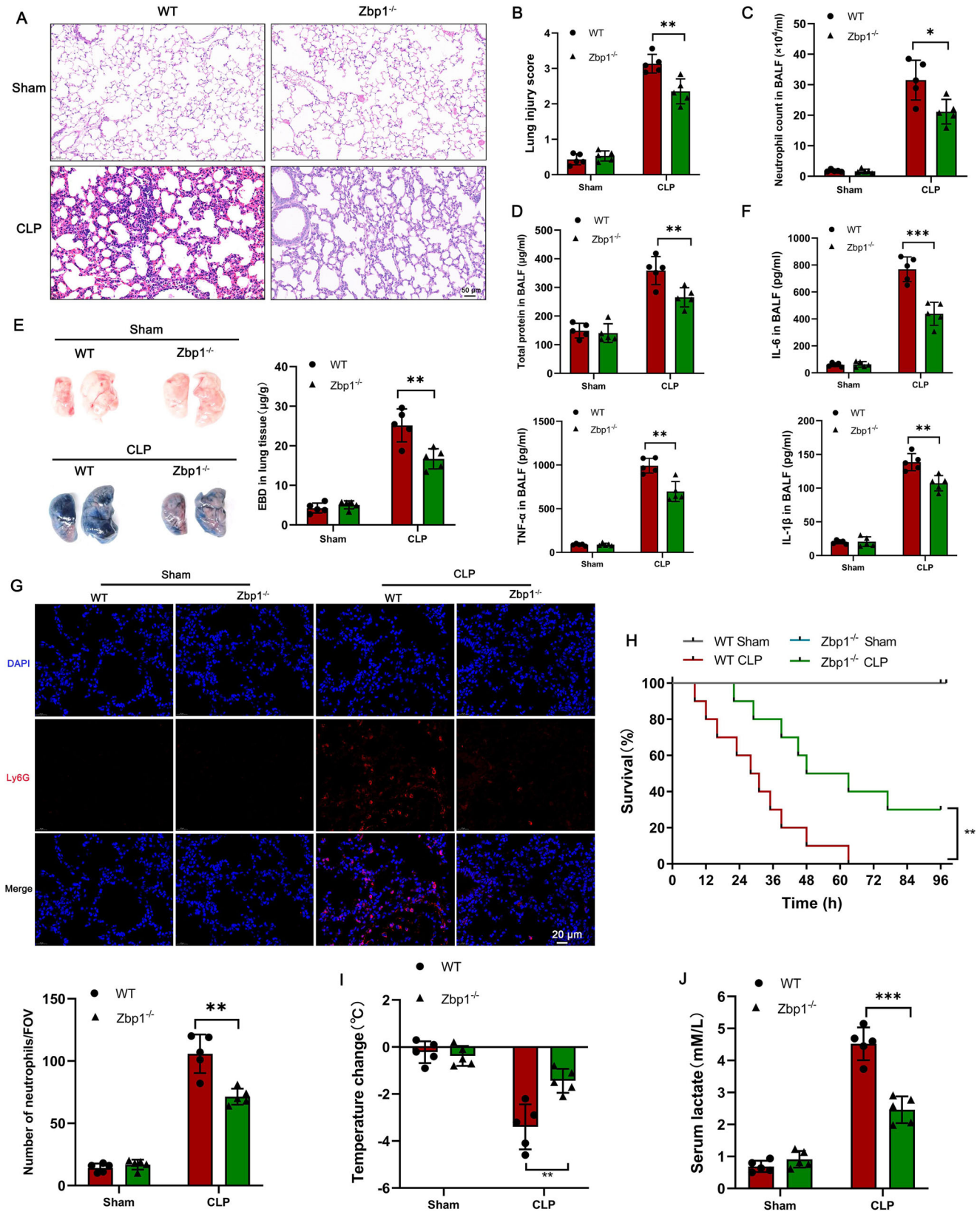

histology demonstrated that in *Zbp1*$^{-/-}$ mice the lungs exhibited less cellular infiltration, reduced edema, and thinner alveolar walls in comparison to WT mice, indicating attenuated lung damage in the absence of ZBP1 (Fig. 2A). The lung injury scores, derived from the pathological examination of these tissues, were considerably lower in the *Zbp1*$^{-/-}$ mice than that in the WT group in sepsis, which underscores the role of ZBP1 in sepsis-induced lung injury (Fig. 2B).

Neutrophil counts in BALF showed a decreased cellular infiltration in the *Zbp1*$^{-/-}$ mice following CLP, suggesting a role of ZBP1 in promoting sepsis-induced cell infiltration into the lungs (Fig. 2C). The BALF protein

Fig. 2 | ZBP1 is involved in sepsis-induced lung injury and mortality. A H&E staining of lung sections from WT and *Zbp1*$^{-/-}$ mice 24 h post-sham or CLP surgery ($n = 5$). Scale bar, 50 μm. **B** Lung injury scores were obtained from the pathological assessment of lung tissues. **C** BALF neutrophil counts were quantitated in each group of mice. **D** Protein levels in BALF, indicative of vascular permeability, were assessed using BCA assay. **E** Evaluation of lung tissue damage and vascular leakage was performed using Evans blue dye extravasation, with quantification illustrating statistically significant differences ($n = 5$). **F** Levels of pro-inflammatory cytokines IL-6, IL-1β, and TNF-α in BALF were quantified using ELISA. **G** Immunofluorescence staining for neutrophil marker Ly6G in lung tissues 24 h post-CLP, with nuclei stained blue and Ly6G in red. The number of neutrophils per high power field (HPF) was quantified ($n = 5$). **H** Kaplan-Meier survival curves illustrate the survival probability of WT and *Zbp1*$^{-/-}$ mice subjected to sham or CLP over 96 h ($n = 10$). **I** Post-CLP core body temperature variations were monitored ($n = 5$). **J** Serum lactate levels were determined 24 h post-CLP using a lactate measurement kit ($n = 5$). Data are represented as mean ± SD, $^{*}P < 0.05$, $^{**}P < 0.01$, $^{***}P < 0.001$.

content, a marker of vascular permeability, was also significantly lower in the *Zbp1*$^{-/-}$ mice (Fig. 2D). Additionally, the *Zbp1*$^{-/-}$ mice showed reduced Evans blue dye extravasation in the lungs compared to the control group following CLP (Fig. 2E).

Pro-inflammatory cytokines in the BALF were quantified using ELISA, revealing that the levels of IL-6, IL-1β, and TNF-α were markedly reduced in the *Zbp1*$^{-/-}$ mice, further suggesting a mitigated inflammatory response in the absence of ZBP1 (Fig. 2F). In addition, immunofluorescence staining for the neutrophil marker Ly6G showed a reduced neutrophil infiltration in the lungs of *Zbp1*$^{-/-}$ mice 24 h post-CLP (Fig. 2G). Post-CLP survival outcomes were significantly improved in *Zbp1*$^{-/-}$ mice, as depicted by Kaplan-Meier survival curves. Over the course of 96 h following the procedure, *Zbp1*$^{-/-}$ mice demonstrated a pronounced survival advantage over the WT mice (Fig. 2H). Furthermore, monitoring of core body temperature changes post-CLP indicated a more stable physiological response in *Zbp1*$^{-/-}$ mice compared to the WT group (Fig. 2I).

Serum lactate levels, measured at 24 h post-CLP, were substantially lower in *Zbp1*$^{-/-}$ mice, which is indicative of enhanced lactate clearance and/or lactate creation. This metabolic parameter correlates with the improved survival seen in these animals, suggesting a better overall outcome in the *Zbp1*$^{-/-}$ group (Fig. 2J). To further evaluate the impact of ZBP1 on organ function, we conducted additional experiments measuring aminotransferases and creatinine levels in the blood samples of these mice. Our findings show that ZBP1 deficiency mitigates CLP-induced liver and kidney damage (Supplementary Fig. 4).

Collectively, these results support the hypothesis that ZBP1 plays a detrimental role in the progression of sepsis-induced ALI, and its absence can lead to a significant reduction in lung injury, better preservation of vascular integrity, decreased inflammation, enhanced metabolic function, and overall improved survival.

scRNA-seq reveals the role of ZBP1 in altering transcriptional profiles of various lung cells following sepsis

To elucidate the role of ZBP1 in sepsis-induced ALI, we collected lung cells from WT and *Zbp1*$^{-/-}$ mice that had undergone either sham or CLP operations. A cohort of 14 samples was subjected to this scrutiny, and following stringent quality control measures (Supplementary Fig. 5). We conducted a thorough scRNA-seq data analysis to dissect the cellular and molecular intricacies resulting from the deficiency of ZBP1 (Fig. 3A). Western blot analysis of lung tissues confirmed the knockout of ZBP1 in *Zbp1*$^{-/-}$ mice and showed an absence of ZBP1 expression post-CLP as opposed to the elevated levels observed in the WT mice, which substantiates the genetic manipulation undertaken in this study (Fig. 3B).

By UMAP analysis, we mapped the intricate cellular landscape of the lung tissue, identifying and counting various cell populations (Fig. 3C). Annotations for cell subpopulations are consistent with those presented in Supplementary Fig. S1C. Our quantitative assessment across the different experimental setups revealed no significant disparities in the relative abundance of each cell type (Fig. 3D).

Next, we observed shifts in the distribution frequencies of different lung cells (Fig. 3E). Further analysis exposed a substantial number of differentially expressed genes (DEGs) across cell types, highlighting several populations that exhibited marked transcriptional alterations when the WT and *Zbp1*$^{-/-}$ mice were contrasted following CLP (Fig. 3F). The integrity of the cell typing was affirmed by a box plot illustrating cell purity (Fig. 3G).

These scRNA-seq data reveal a distinct transcriptional landscape elicited by ZBP1 knockout in lung cells following sepsis and suggest an important role for ZBP1 in transcriptional reprogramming across various lung cells, which may critically affect the cellular response to sepsis and influence the outcomes of ALI.

ZBP1 regulates alveolar macrophage differentiation in sepsis

WT and *Zbp1*$^{-/-}$ mice were subjected to CLP model. t-SNE-based dimensionality reduction and clustering analysis identified three distinct macrophage subpopulations (Macrophage C1, Macrophage C2, and Macrophage C3) across the WT sham, WT CLP, *Zbp1*$^{-/-}$ Sham, and *Zbp1*$^{-/-}$ CLP groups (Fig. 4A). These findings are augmented by a heatmap that delineates the differential expression of the top 15 marker genes within these subgroups, providing a molecular signature of each cluster (Fig. 4B). M1 and M2 polarization states were quantitatively assessed, with violin plots depicting the gene set activity scores that distinguish between the pro-inflammatory and anti-inflammatory macrophage phenotypes within the subpopulations (Fig. 4C).

Through the trajectory analysis, constructed using the Slingshot algorithm[16], we visualized the differentiation pathways of macrophage subsets, indicating a potential reprogramming of macrophage lineage commitment upon ZBP1 knockout (Fig. 4D). CytoTRACE[17] analysis showed the differentiation probability scores, which range from 0 to 1, offering a nuanced view into the relative differentiation states of macrophage subpopulations, where scores nearer to 0 are associated with a higher state of differentiation (Fig. 4E). The two-dimensional t-SNE scatter plot demonstrated the dispersion of macrophage subpopulations, visually supporting the data obtained from the trajectory and CytoTRACE analyses (Fig. 4F). Box plots showcasing CytoTRACE scores elucidate the disparity in differentiation states across macrophage subsets, with Macrophage C3 emerging as the most differentiated macrophage subpopulation (Fig. 4G).

Expression dynamics of the top nine genes with the highest correlation to the differentiation trajectory endpoints were illustrated in line plots, shedding light on the gene expression changes that may underpin macrophage identity and function in this model of ALI (Fig. 4H). The heatmap of the top 30 genes with the highest correlation to differentiation endpoints complemented these findings by offering a broader perspective of the molecular factors involved in macrophage differentiation (Fig. 4I).

Finally, the cell percentage chart provided a visual summary of the different cell cluster distributions among the groups, highlighting the overall impact of ZBP1 knockout on macrophage heterogeneity in the inflammatory milieu of sepsis-induced ALI (Fig. 4J). In conclusion, these data suggest that ZBP1 is a key regulator of macrophage phenotype and function, with its knockout leading to significant changes in macrophage differentiation patterns.

ZBP1 regulates macrophage metabolic and inflammatory status in sepsis

We have delineated distinct macrophage populations, uncovering the impact of ZBP1 disruption on macrophage diversity (Fig. 5A). We observed a marked upregulation of pro-inflammatory genes such as iNOS, TNF, IL6, and SPP1 in the WT CLP group, which was notably mitigated in the *Zbp1*$^{-/-}$ mice (Fig. 5B, C and Supplementary Fig. 6A).

The flow cytometry data further confirmed these findings, indicating a notable decrease in pro-inflammatory SPP1^{+} cells within the ZBP1

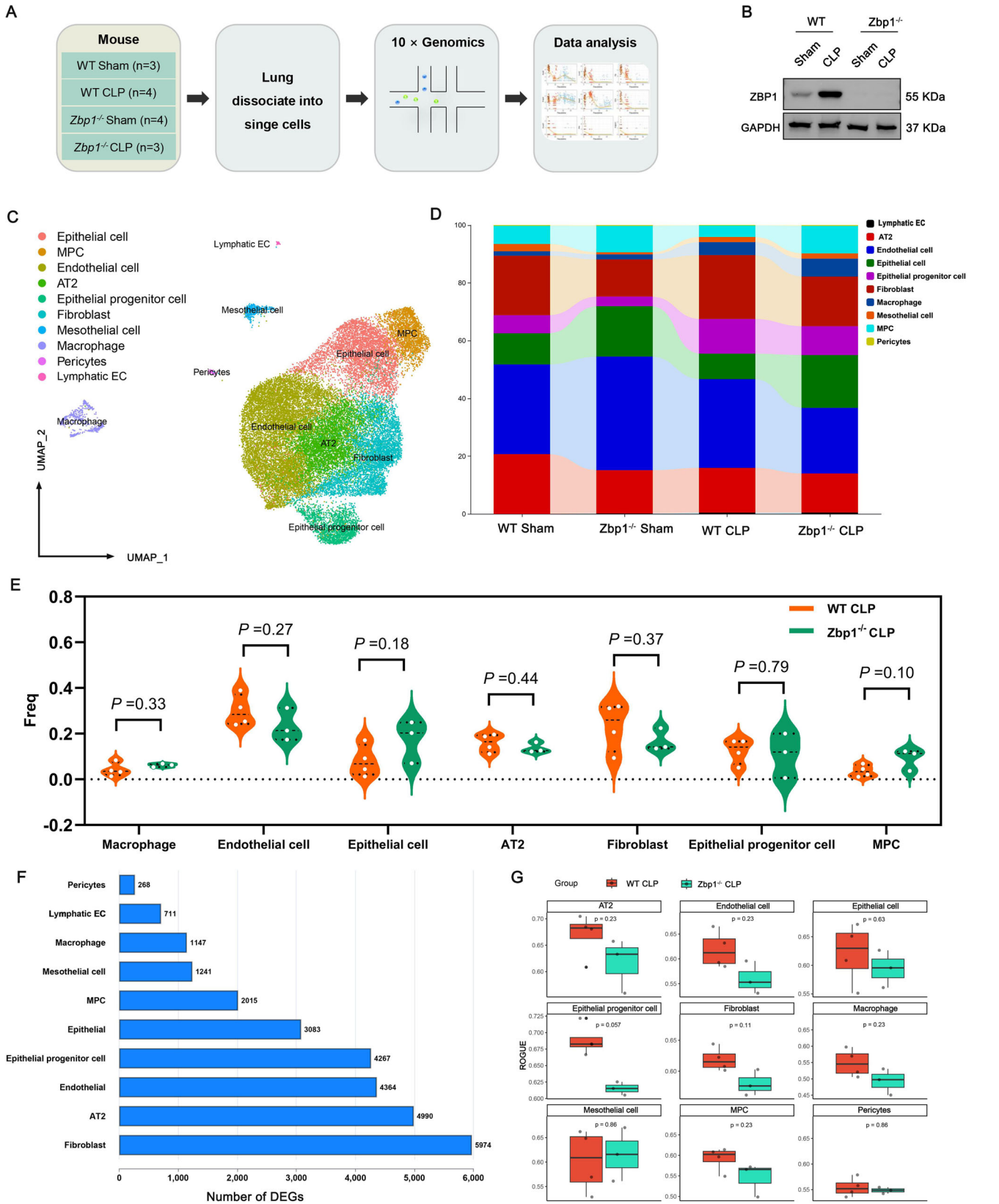

Fig. 3 | scRNA-seq reveals the role of ZBP1 in altering transcriptional profiles of various lung cells following sepsis. A Schematic diagram of sample collection to single-cell sequencing analysis. **B** Western blot analysis for ZBP1 in lung tissues of WT and *Zbp1*$^{-/-}$ mice at 24 h post-CLP and sham procedures. **C** The UMAP plot reveals the heterogeneity of cell populations within lung tissue, with distinct clusters representing ten different cell types as identified by single-cell analysis. **D** The stacked bar chart depicts the proportional distribution of cell types within each experimental group. **E** Violin plots compare the prevalence of cell populations, capturing the variability in cell type frequencies across samples. **F** The bar graph enumerates the differentially expressed genes (DEGs) across cell types, contrasting the transcriptional profiles between WT and *Zbp1*$^{-/-}$ mice post-CLP. **G** Box plots demonstrate the cell-type specificity, confirming the cell purity within the identified populations. Data are presented as the mean ± SD, $^{*}P < 0.05$, $^{**}P < 0.01$, $^{***}P < 0.001$.

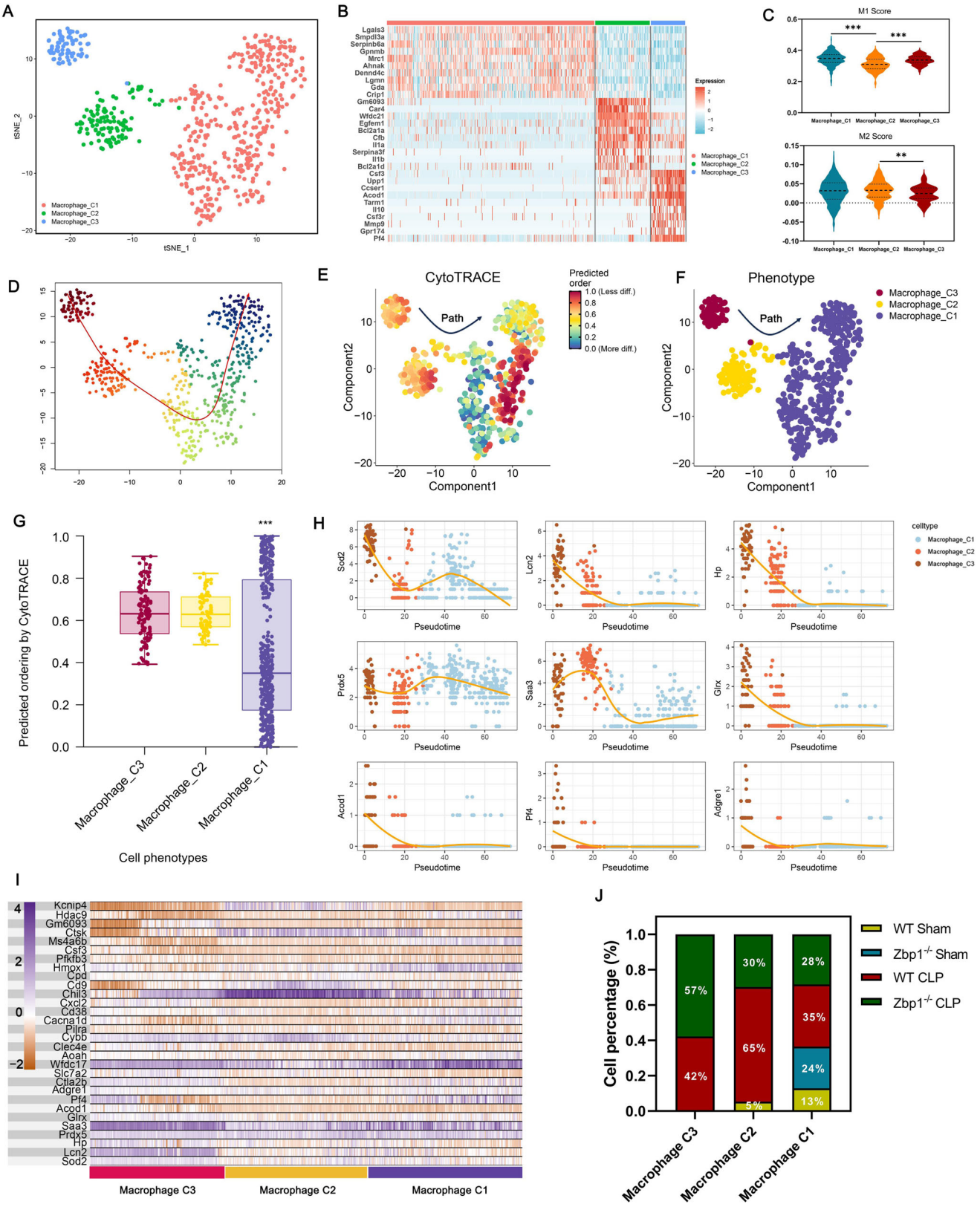

knockout landscape (Fig. 5D). Subsequent analysis of the M1 and M2 polarization scores revealed a tempered pro-inflammatory activation in the macrophages of the *Zbp1*$^{-/-}$ groups (Fig. 5E, Supplementary Fig. 6B, C). This trend continued with the percentage of iNOS^{+} cells in primary macrophages showing a significant increase in the WT CLP group, while ZBP1 knockout reversed this trend, signaling a departure from the classical pro-inflammatory M1 phenotype in sepsis-induced ALI (Fig. 5F, G).

A characteristic feature of M1 activation is its distinct metabolic state, divergent from that of resting macrophages. Cellular metabolic reprogramming is vital for macrophage activation and function. M1

Fig. 4 | ZBP1 regulates alveolar macrophage differentiation in sepsis. A t-SNE-based dimensionality reduction and clustering of macrophages from WT Sham, WT CLP, *Zbp1*$^{-/-}$ Sham, and *Zbp1*$^{-/-}$ CLP groups reveal three macrophage subpopulations: Macrophage C1, Macrophage C2, and Macrophage C3. **B** The heatmap illustrates differential gene expression with the top 15 genes highlighted within the distinct macrophage subgroups. **C** Violin plots depict the M1 and M2 gene set activity scores across the three macrophage subpopulations. **D** Trajectory analysis of macrophage differentiation among subgroups, constructed using Slingshot, is visualized in a scatter plot, with arrows denoting the direction of differentiation and developmental progression. **E** CytoTRACE analysis yields a scatter plot showing the differentiation probability scores of macrophage subpopulations, ranging, and scaled from 0 to 1, predicting relative cellular differentiation states. Scores closer to 0 indicate higher differentiation, whereas scores approaching 1 denote a less differentiated state. **F** A t-SNE scatter plot visualizes the two-dimensional dispersion of macrophage subpopulations. **G** Box plots reveal the variation in differentiation as quantified by CytoTRACE scores among the macrophage subtypes. **H** Line plots illustrate the expression changes of the top 9 genes with the highest correlation to the starting and ending points of the differentiation pathway. **I** The heatmap showcases the expression levels of the top 30 genes with the highest correlation to the differentiation trajectory endpoints. **J** The cell percentage chart depicts the distribution of different cell clusters among the groups. Data are presented as the mean ± SD, $^{*}P < 0.05$, $^{**}P < 0.01$, $^{***}P < 0.001$.

macrophages increase glucose consumption and lactate release while reducing the oxygen consumption rate[18]. Our findings propose that ZBP1 promotes a shift towards an inflammatory M1 phenotype through metabolic reprogramming. To investigate metabolic pathways, we quantified activities across oxidative phosphorylation, glycolysis, and ROS pathways and uncovered a metabolic reconfiguration in *Zbp1*$^{-/-}$ macrophages (Fig. 5H, Supplementary Fig. 6D–G). This was further exemplified by elevated ROS levels, highlighting the metabolic shifts propelled by ZBP1 knockout (Fig. 5I).

Furthermore, we determined the energy state of macrophages by measuring ATP content and demonstrated that ZBP1 knockout alleviated the reduction in cellular energy caused by CLP (Fig. 5J). The electron microscopy analysis of mitochondria illustrated how the structural integrity of these organelles corresponds with metabolic changes. Intact mitochondrial architecture was observed in sham conditions, while CLP resulted in mitochondrial disruption, which was ameliorated by ZBP1 knockout (Fig. 5K). The mitochondrial structural and functional alterations form a crucial component of cellular metabolic reprogramming, with compromised mitochondria driving cells to rely more heavily on anaerobic glycolysis for energy production[19].

The regulatory mechanisms of metabolic reprogramming involve a plethora of signaling pathways and regulators, among which HIF1α has been identified as a key mediator of monocyte metabolic reprogramming during sepsis[20]. At the transcriptomic level, we evaluated the expression of genes, including HIF1-alpha, LDHA, and Slc2a1, revealing alterations in mRNA levels indicative of metabolic adaptation following ZBP1 knockout (Fig. 5L). The modulation of lactate production, a crucial gauge of glycolytic flow, was apparent in the *Zbp1*$^{-/-}$ groups (Fig. 5M). Our findings reveal that ZBP1 knockout diminishes the CLP-induced upregulation of HIF-1α and LDHA protein expression (Fig. 5N).

These findings present an important regulatory influence of ZBP1 in macrophage metabolism and inflammation.

ZBP1 regulates macrophage NLRP3 inflammasome activation and pyroptosis

The analysis of differential gene expression in macrophages indicates that ZBP1 influences the transcriptional landscape under septic stress (Fig. 6A). The enriched KEGG pathways among upregulated genes suggested that ZBP1 knockout significantly impacted biological processes related to inflammation and cell death (Fig. 6B).

The distribution of NLRP3 expression across macrophage subpopulations points to a direct correlation between ZBP1 knockout and inflammasome regulation (Fig. 6C). The expression profiles of pyroptosis-associated markers revealed increased levels of IL-8, NLRP3, AIM2, IL-1β, and caspase-1 in the WT CLP group compared to those in the *Zbp1*$^{-/-}$ CLP group, suggesting that the absence of ZBP1 dampens the inflammatory and pyroptotic response (Fig. 6D). Activity scores for apoptosis pathways across macrophage populations showed the apoptotic potential within each group (Fig. 6E). We observed the co-localization of ZBP1 with NLRP3 within lung macrophages post-CLP, which may trigger the pyroptotic cascade (Fig. 6F). This interaction is further confirmed by a proximity ligation assay (PLA), revealing physical proximity between ZBP1 and NLRP3 in situ, suggesting a potential mechanistic link in inflammasome activation (Fig. 6G).

The expression levels of pro-caspase-1 and its activated form, as well as pro-gasdermin D and its activated form, reveal the proteolytic processing events that culminate in pyroptosis in primary lung macrophages from the WT CLP group (Fig. 6H). Furthermore, the presence of ASC specks points to the assembly of the inflammasome complex, further validating the activation of pyroptotic pathways in these cells (Fig. 6I). Moreover, the identification of pyroptotic cells through TUNEL positivity in macrophages underscores the active execution of cell death pathways, highlighting cells undergoing pyroptosis, particularly in WT CLP macrophages as compared to those in *Zbp1*$^{-/-}$ CLP macrophages (Fig. 6J).

These results demonstrate a critical role of ZBP1 in modulating the activation of the NLRP3 inflammasome and subsequent macrophage pyroptosis.

scRNA-seq reveals macrophages are a dominating regulator in the lung cellular networks in sepsis

CellChat analysis was conducted to investigate the complexities of intercellular interactions. We observed the role of ZBP1 in regulating cell-cell interactions. In *Zbp1*$^{-/-}$ mice, we found significant decreases in the strength of the cell-cell interactions (Fig. 7A, B). Particularly, the interaction strength between macrophages and endothelial cells was diminished in the *Zbp1*$^{-/-}$ group as compared to the WT group (Fig. 7C). Analysis of TNF and IL-1 signaling pathways, which elucidated how the macrophage interactions with other cell types were redistributed, demonstrated that macrophages are a dominating regulator in controlling lung inflammation during injury (Fig. 7D, E).

Further pathway analysis revealed that the IL6 pathways were substantially enriched in the WT CLP group, whereas the ZBP1 knockout led to an upregulation of VEGF pathways and a downregulation of IL6 signaling (Fig. 7F). In addition, the SPP1 signaling pathway was substantially downregulated in the *Zbp1*$^{-/-}$ group (Fig. 7G, H). Studies suggested that SPP1, a cytokine influential in modulating immune responses, acts through various receptors including integrins and CD44, initiating signaling cascades that affect gene expression, cytoskeletal reorganization, and cell survival[21,22].

The t-SNE plots showed differential SPP1 mRNA distribution between the WT and *Zbp1*$^{-/-}$ groups, indicating transcriptional changes in macrophage function due to ZBP1 knockout. Notably, there was a pronounced reduction in SPP1 expression in the lung cells in *Zbp1*$^{-/-}$ animals (Fig. 7I, J). This reduction likely contributes to mitigating macrophage-driven inflammation.

Overall, inflammatory signaling pathways in macrophages from *Zbp1*$^{-/-}$ mice were significantly attenuated in sepsis. They underscore the pivotal role of macrophages, particularly in relation to endothelial cells, as essential mediators of the cellular response to sepsis and point towards macrophage signaling pathways as potential therapeutic targets to alleviate the impact of acute lung injury.

ZBP1 is involved in sepsis-induced endothelial cell damage and dysfunction

In sepsis-induced ALI, PVEC dysfunction results in increased vascular permeability and disruption of the alveolar-capillary barrier, leading to pulmonary edema and impaired gas exchange[23,24]. Our study highlights the crucial role of ZBP1 in maintaining endothelial cell integrity. Based on

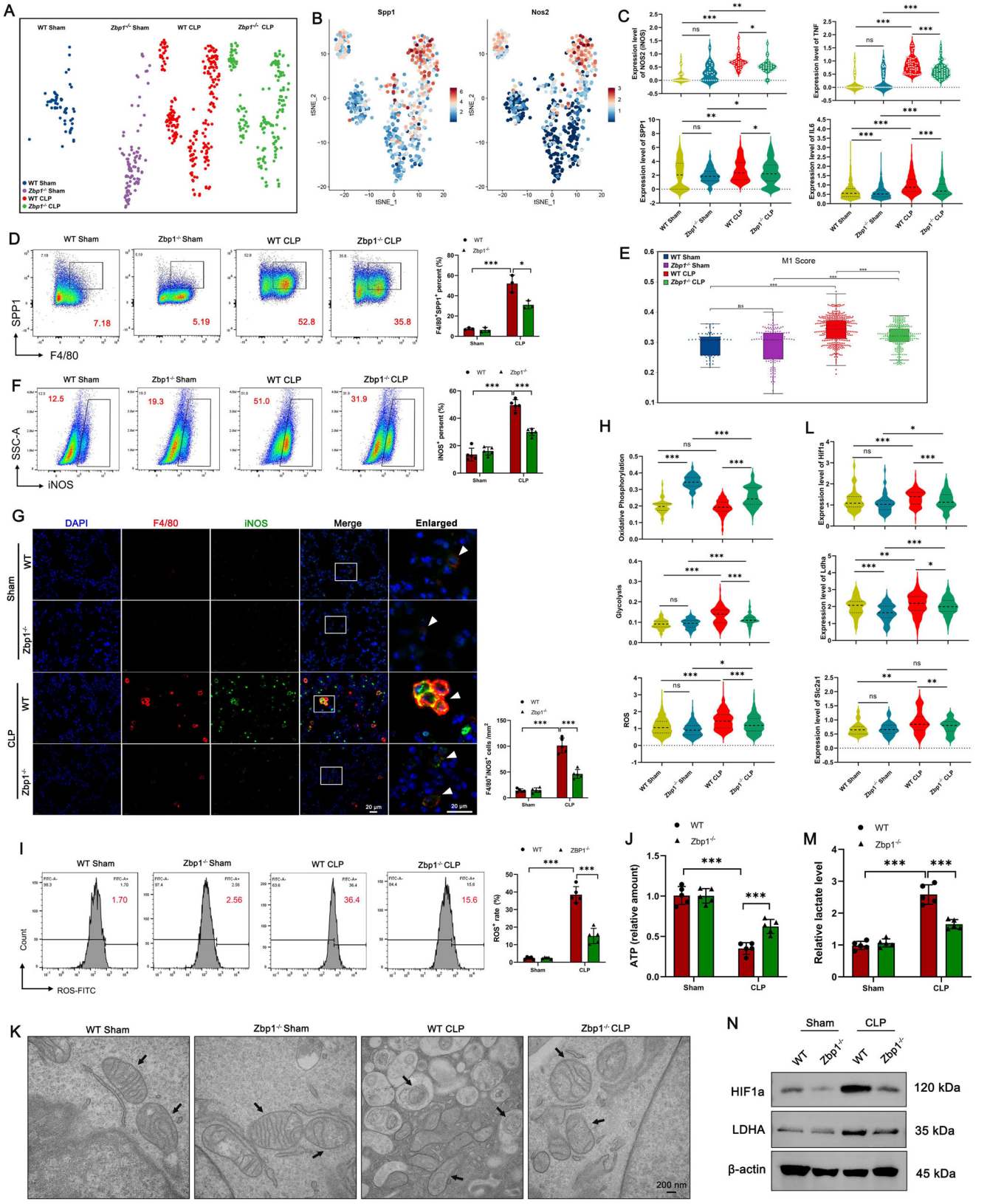

significant differences in gene expression, we have categorized the endothelial cell landscape into three distinct subpopulations (Fig. 8A, B).

We observed a notable increase in the inflammatory endothelial cell E3 subpopulation with high expression of Lcn2 and Saa3 in the CLP group. However, this increase was significantly reduced in the *Zbp1*$^{-/-}$ CLP group (Fig. 8C). Moreover, compared to WT mice, the *Zbp1*$^{-/-}$ mice exhibited a significant downregulation in the expression levels of inflammatory cytokines and cell adhesion molecules, including Icam1, Vcam1, Nfkbia, Ccl2, and Il6, underscoring the modulatory effects of ZBP1 on inflammatory gene expression in response to sepsis (Fig. 8D, E).

Fig. 5 | ZBP1 regulates macrophage metabolic and inflammatory status in sepsis. **A** t-SNE visualization displays the macrophage subpopulations across four experimental groups. **B** The expression distribution of the genes Spp1 and Nos2 within the macrophage subpopulations is illustrated. **C** Single-cell analysis reveals the mRNA expression levels of inflammatory markers, including iNOS, TNF, IL6, and SPP1, across different macrophage groups. **D** Alveolar macrophages isolated from each mouse group were analyzed by flow cytometry to determine the percentage of $SPP1^+$ cells ($n = 3$). **E** Box plots show M1 scoring within macrophages of each group. **F** $iNOS^+$ cells percentage in primary macrophages from each mouse group were detected by flow cytometry ($n = 5$). **G** IF staining was used to visualize F4/80 (red) and iNOS (green) in lung tissues 24 h post-CLP ($n = 5$). White arrowheads point to $F4/80^+$ $iNOS^+$ macrophages. **H** Violin plots present the activity scores for oxidative phosphorylation, glycolysis, and ROS pathways in macrophages of each group. **I** Levels of ROS were measured in macrophages via flow cytometry ($n = 5$). **J** Relative amounts of intracellular ATP in WT and $Zbp1^{-/-}$ macrophages. **K** The structure of mitochondria was evaluated in macrophages using transmission electron microscopy, with black arrows indicating mitochondria ($n = 5$). **L** The mRNA expression levels of HIF1-alpha, LDHA, and Slc2a1 in single-cell transcriptomes. **M** Lactate levels in primary macrophages from each group were measured with a lactate assay kit. **N** Protein expression levels of HIF1-a and LDHA in macrophages were assessed by Western blot. All results are based on three independent experiments. Data are represented as mean ± SD, $^*P < 0.05$, $^{**}P < 0.01$, $^{***}P < 0.001$.

Consistently, in the WT group, sepsis decreased the protein expression of endothelial junction proteins VE-cadherin and claudin 5 and increased the expression of Icam1 and Vcam1. In contrast, ZBP1 knockout mitigated the CLP-induced decrease in VE-cadherin and claudin 5 expression and the increase in Icam1 and Vcam1 (Fig. 8F). Thes results suggest that ZBP1 contributes to endothelial barrier dysfunction by reducing endothelial adhesion and tight junction proteins while increasing adhesion molecule expression.

Furthermore, we observed reduced endothelial cell apoptosis in the $Zbp1^{-/-}$ CLP group by quantitating Annexin V/PI staining endothelial cells (Fig. 8G). Lung tissue analysis provided further support for these findings, as evidenced by fewer TUNEL-positive endothelial cells in $Zbp1^{-/-}$ CLP mice compared to WT CLP mice (Fig. 8H).

These findings demonstrate that ZBP1 involves in sepsis-induced endothelial cell damage and dysfunction, positioning ZBP1 as a therapeutic target to alleviate endothelial injury in inflammatory and septic conditions.

Discussion

The current study using $Zbp1^{-/-}$ mice revealed that ZBP1 plays an important role in promoting the development and progression of ALI following systemic inflammatory response in sepsis. ZBP1 induces mitochondrial damage and glycolysis, which modulates macrophage metabolic status. This, in turn, increases the differentiation of macrophages into pro-inflammatory states. Furthermore, it induces the activation of the NLRP3 inflammasome in macrophage and subsequent pyroptosis. These actions collectively enhance the inflammatory signaling pathways between macrophages and other cells. Additionally, ZBP1 also plays a role in inducing endothelial cell dysfunction, which causes endothelium damage and increased permeability. Taken together, these multiple functions of ZBP1 significantly contribute to the severity of sepsis-induced ALI and higher mortality (Fig. 9).

The results underscore the complex interplay between cellular components within the lungs during sepsis. Subsequently, we observed elevated expression of ZBP1 across multiple cell types, suggesting ZBP1 is an important regulator in the inflammatory response[25]. Spontaneous activation of ZBP1 leads to the necroptotic cell death of keratinocytes or intestinal epithelial cells, which results in sterile autoinflammation[26,27]. Importantly, in sham condition, there was no difference in the lung status between WT and $Zbp1^{-/-}$ mice. However, in the context of sepsis, ZBP1 knockout significantly improved outcomes by reducing the inflammatory factors, alleviating endothelial dysfunction, and enhancing the survival rates of the mice.

The modulation of immune cell metabolism in sepsis impacts their immune functions[19]. M1 macrophages, noted for their pro-inflammatory functions, enhance glucose uptake and lactate secretion while reducing oxygen consumption[18,28]. Our study utilized single-cell transcriptomics to reveal a notable downregulation of oxidative phosphorylation (OXPHOS) and an enhancement of glycolysis in macrophages during sepsis, which was accompanied by an increase in ROS production. Notably, this increase in ROS was substantially reduced in $Zbp1^{-/-}$ mice.

Mitochondrial dysfunction shifts energy production from OXPHOS to anaerobic glycolysis to satisfy ATP demands[29]. The inhibition of the mitochondrial respiratory chain is linked to an increase in ROS production, underlining the relationship between OXPHOS suppression and ROS generation[30]. Metabolic reprogramming is part of the mitochondrial stress response, allowing a damaged mitochondrial network to recover by switching from oxidative metabolism to aerobic glycolysis, thereby increasing the production of ATP and NADPH for energy and antioxidant defense[31,32]. The metabolic profile of immune cells is crucial for determining their inflammatory phenotype. In this study, we observed significant metabolic reprogramming in lung macrophages during the septic response, contributing to the progression of ALI. Similarly, research suggests that liver-resident Kupffer cells also undergo metabolic reprogramming under stress conditions, characterized by alterations in mitochondrial function or lactate production, which may shift their phenotype toward inflammation regulation and influence the progression of liver injury[33,34].

Our study found that ZBP1 knockout significantly alleviated mitochondrial dysfunction and ROS accumulation in macrophages during sepsis. Research shows that ZBP1 acts as an innate immune sensor for mitochondrial genome instability, collaborating with cGAS to maintain IFN-I signaling, which in turn promotes mitochondrial dysfunction and cardiac injury[11]. Overall, our results provide new evidence for the role of ZBP1 in regulating macrophage metabolic reprogramming through mitochondrial modulation in sepsis.

HIF-1α critically regulates glycolysis by upregulating the transcription of glycolytic enzymes and membrane transport proteins, thereby enhancing glucose flux and glycolysis[35]. The products of glycolysis further regulate HIF-1α activity and metabolic reprogramming, which in turn promotes a pro-inflammatory phenotype in macrophages[36]. In this study, we found that ZBP1 deficiency reduces lactate production and glycolysis induced by sepsis, as well as the elevated expression and transcriptional activity of HIF-1α. The increase in glycolysis and the accumulation of succinate enhance the production of IL-1β[37]. Consequently, the reduced release of inflammatory cytokines such as TNF-α and IL-1β following inflammasome activation in ZBP1-deficient macrophages may be influenced by a combination of glycolytic and mitochondrial signaling pathways.

It has been reported that ZBP1 on mitochondria, potentially a key downstream event of telomere stress signaling, leads to MAVS activation[38]. MAVS facilitates the recruitment of NLRP3 to mitochondria, thereby promoting the production of IL-1β and the activation of the NLRP3 inflammasome[39]. Studies have shown that upon pathogenic stimulation, ZBP1, as a specific sensor, activates the NLRP3 inflammasome[40,41]. Our findings suggest that the absence of ZBP1 dampens inflammatory and pyroptotic responses, as indicated by lower expression levels of pyroptosis-associated markers, including IL-8, NLRP3, AIM2, IL-1β, and caspase-1 in the $Zbp1^{-/-}$ mice. Additionally, the interaction between ZBP1 and NLRP3 in lung macrophages following CLP points to a potential mechanism triggering the pyroptotic cascade. Our study underscores the critical role of ZBP1 in modulating inflammasome activity and pyroptosis.

The significant amelioration of endothelial cell damage and dysfunction in $Zbp1^{-/-}$ mice indicates the importance of ZBP1 in damaging endothelial stability and alveolar-capillary barrier integrity during sepsis. The ZBP1 knockout mitigated changes in endothelial junction integrity caused by sepsis, particularly preserving the expression of VE-cadherin and Claudin-5, while reducing the expression of adhesion molecules. Recent studies have identified ZBP1 as an innate sensor during infection, regulating cell death, inflammasome activation, and pro-inflammatory responses[12,42]. Our findings indicate that the improvement in endothelial cell damage

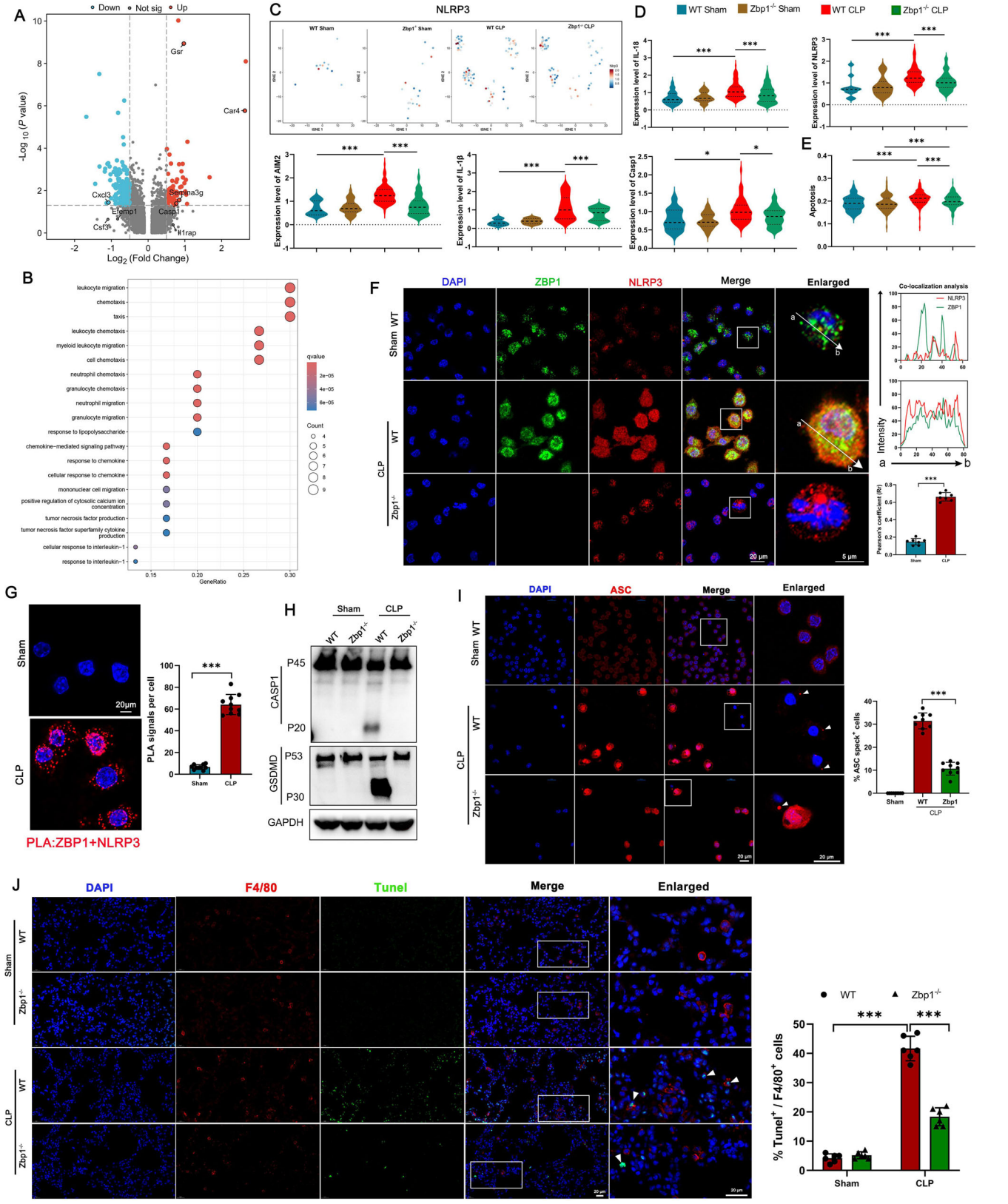

mechanisms in sepsis by ZBP1 knockout is due to reduced programmed cell death, leading to less cellular damage.

On the other hand, we found that ZBP1 knockout reduces the upregulation of inflammatory genes such as Icam1, Nfkbia, Ccl2, and Il6 in endothelial cells during sepsis. This regulation suggests that ZBP1 is involved in the inflammatory cascade during inflammation[12], and our results indicate that ZBP1 knockout may weaken the inflammatory signaling pathways between macrophages and endothelial cells, potentially by reducing the release of inflammatory factors, thereby mitigating the inflammatory cascade.

Fig. 6 | ZBP1 regulates macrophage NLRP3 inflammasome activation and pyroptosis. **A** Volcano plot highlighting differential gene expression in macrophages between WT CLP and *Zbp1*$^{-/-}$ CLP mice. Upregulated genes are denoted in red, while downregulated genes are shown in blue. **B** Bubble chart illustrates enriched KEGG pathways among upregulated differentially expressed genes. **C** t-SNE visualization displays the expression distribution of NLRP3 across macrophage subpopulations in the four groups. The expression level is represented by the intensity of red color, with 0 values not displayed. **D** single-cell analysis showing the mRNA expression levels of pyroptosis-related genes, including IL-8, NLRP3, AIM2, IL-1β, and caspase-1. **E** Violin plots present the activity scores for apoptosis pathways in macrophages from each group. **F** Confocal microscopy was used to observe the co-localization of ZBP1 (green) and NLRP3 (red) in lung macrophages from both CLP and sham groups ($n = 5$). Co-localization analysis was performed using ImageJ software. Scale bar, 20 μm. **G** Proximity ligation assay (PLA) employed specific antibodies against ZBP1 and NLRP3, with DAPI staining indicating nuclei. Scale bars, 20 μm. **H** Western blot analysis assessed the protein expression levels of pro-caspase-1 (P45) and its activated form (P20), as well as pro-gasdermin D (GSDMD, P53) and its activated form (P30), in primary lung macrophages from each group. **I** Pyroptosis was evaluated by detecting ASC specks using IF. **J** IF staining detected F4/80 (red) and TUNEL (green) in lung tissues 24 h post-CLP ($n = 5$). White arrowheads highlight macrophages positive for both TUNEL and F4/80. Data are represented as mean ± SD, $^{*}P < 0.05$, $^{**}P < 0.01$, $^{***}P < 0.001$.

However, the current study has limitations. Our research mainly focused on macrophages and endothelial cells, and future studies are needed to determine the specific role of ZBP1 in other cell types involved in inflammation and disease pathogenesis. Additionally, although we identified that ZBP1 knockout reduces mitochondrial damage and observed potential changes in glycolysis, glycolysis was not the main pathway explored in this study. Future studies should include experiments using glycolysis inhibitors, such as metformin, to further clarify the role of glycolysis in ZBP1-mediated effects.

In conclusion, our single-cell transcriptomic analysis of acute lung injury in sepsis provides a foundational dataset for studying lung damage in sepsis. Our study shows that ZBP1 knockout reduces mitochondrial damage and inhibits glycolysis, leading to altered macrophage metabolism and reduced differentiation into pro-inflammatory states. ZBP1 knockout also diminishes macrophage pyroptosis by inhibiting NLRP3 inflammasome activation, weakening inflammatory signaling across cells. Additionally, ZBP1 knockout helps alleviate endothelial dysfunction and cellular damage, offering potential therapeutic implications for managing sepsis-related inflammation. Further understanding of the interactions between ZBP1, metabolic reprogramming, mitochondrial homeostasis, and immune response through single-cell transcriptomics and validation may bring new insights into the pathogenesis of sepsis.

Materials and methods

Animal strains

The experimental protocols involving animals were rigorously reviewed and received approval from the Institutional Animal Care and Use Committees at the University of Pittsburgh and the VA Pittsburgh Healthcare System. The University of Pittsburgh's animal protocol number is IS0002501524045015, and the VA Pittsburgh Healthcare System's protocol number is 1617201. C57BL/6 wild-type (WT) mice were sourced from Jackson Laboratories. ZBP1 knockout (*Zbp1*$^{-/-}$) mice were obtained from the University of Pittsburgh.

Cecal ligation and puncture model

For the procedure, mice received an intraperitoneal injection of 50 mg/kg ketamine and 5 mg/kg xylazine for anesthesia. Following a 1.5 cm abdominal incision, the cecum was externalized, securely ligated with 4-0 silk sutures, and punctured once using a 22-gauge needle to create a through-and-through puncture. The abdominal incision was then sutured closed with 4-0 silk, and the cecum was repositioned internally. Post-surgery, the mice were monitored for mortality at 6-h intervals during survival studies. For specific experiments, mice were euthanized 24 h post-CLP to collect blood, BALF, and lung tissues.

Apoptosis analysis

To evaluate cell apoptosis, we followed the procedures outlined in the Annexin V-FITC/PI Cell Apoptosis Detection Kit (BD Biosciences, East Rutherford, NJ, USA). Cells were treated with Annexin V-FITC binding solution and propidium iodide (PI). Data from these assays were analyzed using FlowJo software (version 10.0.7, Tree Star, Inc., Ashland, OR, USA).

Western blot analysis

Protein extraction was performed using RIPA lysis buffer supplemented with protease inhibitors (Sigma), and protein concentration was determined using a BCA protein assay kit (Thermo). We loaded 30 μg of total protein into each lane and separated them on 10% SDS-PAGE, then transferred onto PVDF membranes (Millipore, Billerica, MA, USA). The membranes were blocked using 5% non-fat milk for 1 h at room temperature, followed by overnight incubation with specific primary antibodies at 4 °C. The primary antibodies included CASP1, GSDMD, ZBP1, VE-cadherin, Claudin 5, VCAM1, ICAM1, HIF1a, LDHA, β-actin, and GAPDH. Details on these antibodies are provided in Supplementary Table 1. After incubation with HRP-conjugated secondary antibodies, protein bands were visualized using enhanced chemiluminescence (ECL) reagents (Merck Millipore). Images of the bands were captured using a ChemiDoc imaging system (Bio-Rad).

Hematoxylin and eosin (H&E) staining and lung injury scoring

Lung samples were fixed in 4% paraformaldehyde, embedded in paraffin, and then sectioned into 5-μm slices. These sections underwent H&E staining using standard histopathological techniques. Observations of histopathological changes were made using a light microscope. The extent of lung injury, which included criteria such as atelectasis, alveolar and interstitial inflammation, hemorrhage, edema, necrosis, and overdistension, was assessed in six sections from the lower lobes. The scoring was as follows: 0 indicated no injury; 1 indicated injury to 25% of the field; 2 to 50%; 3 to 75%; and 4 indicated diffuse injury throughout the field. Independent pathologists, who were blinded to the experimental groups, conducted the lung injury evaluations.

Immunofluorescence staining

Cells or tissues are fixed at room temperature in 4% paraformaldehyde for 30 min, permeabilized with 0.1% Triton X-100 for 5 min, and then blocked with 5% BSA at room temperature for another 30 min. Overnight incubation at 4 °C with primary antibodies against Ly6G, CD31, F4/80, iNOS, NLRP3, and ZBP1 follows. The next day, the slides are incubated with fluorescently labeled secondary antibodies (1:100) in the dark for 1 h. Cell nuclei are stained with DAPI for 5 min. Samples are then observed and imaged under a Nikon A1R confocal microscope.

Proximity ligation assay (PLA)

For the PLA, cells are seeded in confocal dishes, washed with PBS, and fixed with 4% formaldehyde for 15 min. Blocking is done with 5% BSA for 30 min, followed by overnight incubation at 4 °C with antibodies against ZBP1 and NLRP3. Probe incubation, ligation, and amplification steps are performed according to the manufacturer's instructions (Duolink Detection Kit, DUO92102-1KT, Sigma-Aldrich). Nuclei are stained with DAPI and slides are mounted. PLA samples are imaged and analyzed using a 60x objective on a Nikon A1R confocal microscope.

Lung microvascular permeability assessment

Lung microvascular permeability is evaluated using Evans blue dye extravasation. Thirty minutes before euthanasia, mice receive an intravenous injection of Evans blue dye (20 mg/kg, Sigma). Lungs are perfused with PBS to

remove intravascular dye and then harvested. The lung tissue is homogenized and incubated overnight at 37 °C with PBS containing 16.7% formamide. The homogenate is filtered through a 70-μm mesh and plated in a 96-well plate. Absorbance at 620 nm and 740 nm is measured, and the amount of extravasated Evans blue dye is calculated based on a standard curve[43].

Single-cell suspension preparation, library construction, and sequencing

Twenty-four hours post-surgery, all mice were euthanized, and lung tissues were swiftly excised. Under sterile conditions, tissues were washed twice with ice-cold PBS supplemented with 0.04% BSA. Using sterile surgical

Fig. 7 | scRNA-seq reveals macrophages are a dominating regulator in the lung cellular networks in sepsis. A Network diagrams demonstrate the differences in the number of ligand-receptor pairs (left) and communication probabilities (right) between cell subpopulations within WT CLP and *Zbp1*$^{-/-}$ CLP groups. The peripheral solid circles represent various cell subpopulations, with the circle size corresponding to the number of ligand-receptor pairs. Blue lines indicate stronger communication in the WT CLP group, while red lines denote stronger communication in the *Zbp1*$^{-/-}$ CLP group. The line thickness reflects the magnitude of communication change. **B** Heatmaps depict the differential number of interactions (left) and interaction strengths (right) among all cell subpopulations between the two groups. The *y*-axis represents the ligand-expressing cells, the *x*-axis the receptor-expressing cells, and the color scale the difference in communication probability. Bars at the top and right represent the cumulative differences in communication probability along each axis. **C** Graphical representations of macrophage interactions as ligand cells affecting other cell subpopulations. The size of each circle denotes the number of ligand-receptor pairs within that subpopulation, and the width of the lines represents the probability of communication, with thicker lines indicating higher probabilities. **D** Hierarchical plots of the TNF signaling pathway network and (**E**) IL1 signaling pathway network show autocrine and paracrine signaling interactions within specified cell subpopulations and the remaining cell subpopulations, respectively. Each colored circle represents a cell subpopulation, solid circles for ligand cells, and hollow circles for receptor cells. The line thickness reflects the cell communication probability. **F** Bar charts illustrate the differences in enriched signaling pathways between the *Zbp1*$^{-/-}$ CLP and WT CLP groups. Pathways on the *y*-axis are colored red for significantly stronger communication in the WT CLP group. Blue pathways indicate stronger communication in the *Zbp1*$^{-/-}$ CLP group. **G** A bubble plot represents the probability of macrophage interactions as ligand cells with other cell types between the *Zbp1*$^{-/-}$ CLP and WT CLP groups. The *x*-axis labels the cell pairs, differentiated by color (blue for *Zbp1*$^{-/-}$ CLP, red for WT CLP), and the *y*-axis represents ligand-receptor pairs. **H** A bubble plot visualizes the probability differences in macrophage-to-macrophage ligand-receptor pairs between the *Zbp1*$^{-/-}$ CLP and WT CLP groups. **I** t-SNE plots show the distribution of SPP1 mRNA expression between the groups, with zero values in gray and a gradient indicating the expression level. **J** Western blot analysis was performed to assess the protein expression of SPP1 in macrophages from WT CLP and *Zbp1*$^{-/-}$ CLP mice. All results are based on three measurements. Data are represented as mean ± SD, $^{*}P < 0.05$, $^{**}P < 0.01$, $^{***}P < 0.001$.

scissors, the clean tissues were carefully minced into approximately 0.5 mm^3 fragments and then placed in freshly prepared digestion solution. The digestion was conducted at 37 °C for 30 min, with intermittent stirring every 10 min. The resulting cell suspension was filtered twice through a BD 70-μm cell strainer, followed by centrifugation at 4 °C at 400×*g* for 5 min. The pellet was resuspended in an appropriate volume of medium, mixed with an equal volume of red blood cell lysis buffer, and incubated at 4 °C for 5 min. Afterward, the sample was centrifuged at 400×*g* for 5 min, and the supernatant was discarded. The pellet was washed once with medium and centrifuged again at 400×*g* for 5 min. After discarding the supernatant, the sample was resuspended in 100 μl of medium. The freshly prepared single-cell suspension was adjusted to a concentration of 30,000 cells per sample. Library construction followed the manufacturer's instructions for the 10x Genomics Chromium Next GEM Single Cell 3' Reagent Kit v3.1 (Catalog No. 000388). The libraries were sequenced using high-throughput sequencing on the NovaSeq 6000 platform.

Single-cell data processing and cell identification

We utilized Cell Ranger software (version 5.0.0) from 10x Genomics to demarcate cell barcodes and assign sequence reads to the corresponding genomic and transcriptomic profiles. The output was a matrix representing gene counts across cells. Quality control was enforced using critical metrics: each cell was required to express between 500 and 7000 unique genes (nFeature_RNA), have fewer than 50,000 total RNA counts (nCount_RNA), and contain less than 5% mitochondrial genes.

For data analysis, we adopted the Seurat pipeline (version 5.0.3), employing dimensionality reduction and unsupervised clustering for quality checks. Data normalization was performed using NormalizeData and ScaleData functions from Seurat[44], selecting 2,000 highly variable genes for detailed examination via FindVariableFeatures, and employing 19 principal components for further dimensionality reduction.

To mitigate batch effects, we applied the Harmony algorithm (version 0.1)[45]. Cluster dimensionality was adjusted using "dims = 1:19, resolution = 0.5" parameters in RunUMAP and FindClusters. Initial cell type prediction for each cluster was conducted using scMayoMap software (version 0.1.0)[46]. For refinement, the top 50 differentially expressed genes from each cluster were analyzed using CellMarker 2.0, PanglaoDB, and the ACT database, enhancing the accuracy of cell type assignments. In terms of marker gene presentation, we focused on genes that showed cluster-specific expression from the top 50 DEGs of each cluster, ensuring a balance between the breadth of candidate genes and the focus on those most differentially expressed, thus likely to be biologically significant and reliable markers of specific cell types or states.

ROGUE index

To assess the heterogeneity within different clusters, we employed the ROGUE (version 1.0)[47], which quantifies the diversity of cell states or types in each cluster. The ROGUE index was calculated using this package for each cluster identified in our single-cell RNA sequencing data. Subsequently, we performed a statistical significance assessment of the observed ROGUE values between the groups of interest.

M1 and M2 functional scores in macrophages

Using the AddModuleScore function on our single-cell RNA sequencing dataset, we quantified the M1 and M2 functional scores for each macrophage cell, indicative of pro-inflammatory and anti-inflammatory activities, respectively. These scores represent the relative expression levels of genes linked to these specific functional modules. A higher score denotes greater enrichment of the corresponding functional state. We based our selection of gene sets for M1 and M2 modules on the macrophage functional gene set[15], which encompasses established markers and signature genes characterizing these distinct functional states.

Metabolic pathway analysis

To evaluate differences in metabolic pathways among various cell groups, we downloaded 98 metabolism-related pathways from the GSEA database and calculated the pathway scores for distinct cell clusters using the AddModuleScore function in Seurat. For identifying significantly altered metabolic pathways, we applied the Wilcoxon test ($P < 0.05$) to compare pathways between Zbp1$^{-/-}$ and WT mice post-CLP. Bonferroni correction was used to adjust the p-values for multiple comparisons.

Pathway enrichment analysis

To unravel the functional mechanisms and biological pathways linked to different cell clusters, we conducted Gene Ontology (GO) and Kyoto Encyclopedia of Genes and Genomes (KEGG) pathway enrichment analyses using Metascape. For each cell cluster, we identified the top 150 differentially expressed genes (DEGs) based on their natural logarithmic fold change (logFC), with a threshold of logFC > 0.25. These DEGs are the most notably upregulated genes within each cluster relative to the general population. Our focus on these top DEGs was aimed at pinpointing the crucial functional pathways and biological processes distinct to each cell cluster.

Inference of cellular differentiation trajectories

To elucidate potential lineage differentiation and developmental trajectories within our single-cell RNA sequencing dataset, we utilized two complementary computational approaches: CytoTRACE (version 0.3.3)[17] and Slingshot (version 2.0.0)[16]. By computing a CytoTRACE score for each cell, we can determine its relative position along a differentiation trajectory. Cells with higher CytoTRACE scores are typically less differentiated, suggesting a proximity to the start of the differentiation process, whereas cells with lower scores are more differentiated, indicative of nearing the trajectory's end.

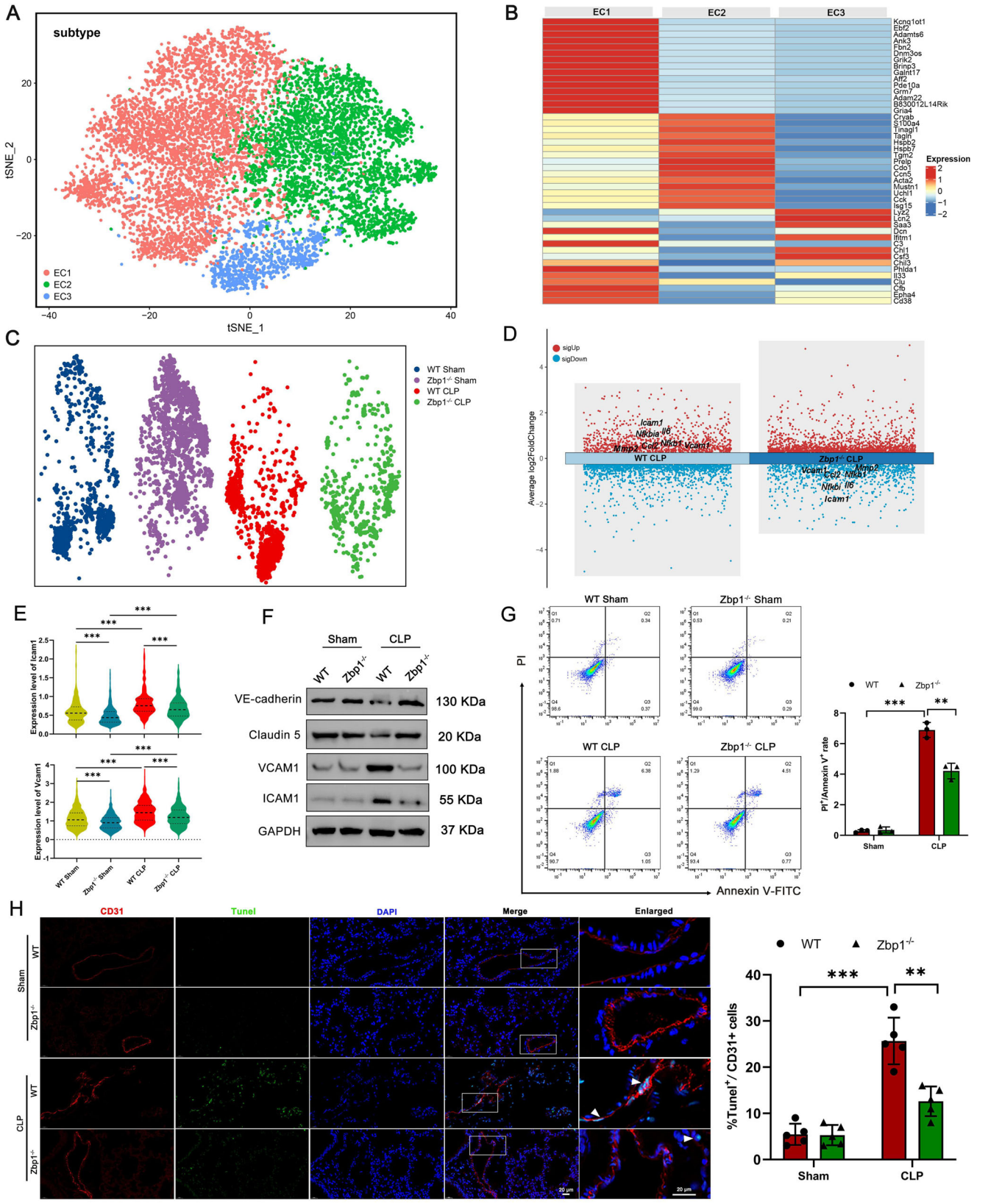

This method provides insights into the spectrum of cellular states and potential lineage connections within our dataset.

To further explore the dynamic changes in gene expression and the potential branching patterns of cellular differentiation, we applied Slingshot, a highly flexible and robust method for inferring pseudotime trajectories. Slingshot utilizes a novel approach based on principal curves and graph theory to construct continuous developmental trajectories that capture the progression of cells through different states or lineages.

Fig. 8 | ZBP1 is involved in sepsis-induced endothelial cell damage and dysfunction. **A** t-SNE analyses demonstrate dimensionality reduction and distinct clustering among endothelial cells from the WT Sham, WT CLP, *Zbp1*$^{-/-}$ Sham, and *Zbp1*$^{-/-}$ CLP groups, revealing three subpopulations. **B** The heatmap details the expression levels of the top 15 marker genes within each endothelial cell subgroup, with red signaling higher expression and blue indicating reduced expression. **C** t-SNE visualizations underscore distinct patterns of subpopulation clustering within the four groups. **D** The volcano plot of the endothelial subpopulations between *Zbp1*$^{-/-}$ CLP and WT CLP groups features genes with differential expression; upregulated genes are marked by red dots and downregulated genes by blue. **E** Single-cell analysis shows a notable increase in mRNA levels of Icam1 and Vcam1 in the WT CLP groups, which are diminished in the *Zbp1*$^{-/-}$ mice. **F** Western blot analysis depicts the differential protein expression of VE-cadherin, claudin 5, Icam1, and Vcam1 in primary mouse endothelial cells, with GAPDH serving as a loading control. **G** Endothelial cell apoptosis is assessed by Annexin V/PI staining through flow cytometry ($n = 3$). **H** Immunofluorescence staining for CD31 (red) and TUNEL (green) in lung sections post-CLP at 24 h ($n = 5$). Data are represented as mean ± SD, $^{*}P < 0.05$, $^{**}P < 0.01$, $^{***}P < 0.001$.

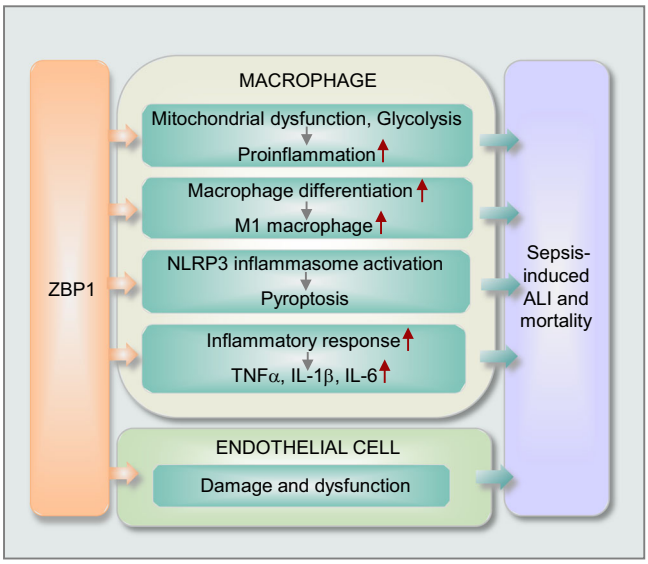

Fig. 9 | Summary model. The current study using *Zbp1*$^{-/-}$ mice revealed that ZBP1 plays an important role in promoting the development and progression of ALI following systemic inflammatory response in sepsis. ZBP1 induces mitochondrial damage and glycolysis, which modulates macrophage metabolic status. This, in turn, increases the differentiation of macrophages into pro-inflammatory states. Furthermore, it induces the activation of the NLRP3 inflammasome in macrophage and subsequent pyroptosis. These actions collectively enhance the inflammatory signaling pathways between macrophages and other cells. Additionally, ZBP1 also plays a role in inducing endothelial cell dysfunction, which causes endothelium damage and increased permeability. Taken together, these multiple functions of ZBP1 significantly contribute to the severity of sepsis-induced ALI and higher mortality.

Cell-cell communication and interactions

To explore the complex network of cell-cell communication among the distinct cell populations identified in our single-cell RNA sequencing data, we utilized the CellChat package (version 1.5.0)[48]. Initially, we created a CellChat object using the normalized gene expression matrix along with cell meta-data, which included cell type labels for each cell. This object forms the basis for all subsequent analyses and stores essential information for deducing cell-cell interactions. We then implemented the CellChat pipeline to identify potential ligand-receptor interactions among the cell populations. CellChat uses a curated database of known ligand-receptor pairs, analyzing their expression patterns across cell types to predict intercellular communication networks. It quantifies communication probabilities and signaling strengths for each pair, offering a detailed measure of the interactions' likelihood and intensity.

Statistical analysis

All data were processed using R Studio (version 4.3.3) or GraphPad Prism (version 9.5). The results are presented as the mean ± SD, based on data from at least three independent experiments. Survival curves were generated using the Kaplan-Meier method and differences were evaluated with the log-rank test. Statistical significance was established at a threshold of $P < 0.05$. For comparative analysis, Student's *t*-test was employed for two-group comparisons, while one-way ANOVA was used for analyses involving multiple groups.

Reporting summary

Further information on research design is available in the Nature Portfolio Reporting Summary linked to this article.

Data availability

The source data for the graphs and charts in the main figures are provided in Supplementary Data 1–4. Uncropped original blot/gel images from the main figures are available in Supplementary Fig. 7. The single-cell RNA sequencing data have been deposited in the GSE278767. All other data can be obtained from the corresponding author upon reasonable request.

Received: 27 July 2024; Accepted: 14 October 2024;
Published online: 21 October 2024

References

1. Meyer, N. J., Gattinoni, L. & Calfee, C. S. Acute respiratory distress syndrome. *Lancet* **398**, 622–637 (2021).
2. Tomazini, B. M. et al. Effect of dexamethasone on days alive and ventilator-free in patients with moderate or severe acute respiratory distress syndrome and COVID-19: the CoDEX randomized clinical trial. *JAMA* **324**, 1307–1316 (2020).
3. Karalapillai, D. et al. Effect of intraoperative low tidal volume vs conventional tidal volume on postoperative pulmonary complications in patients undergoing major surgery: a randomized clinical trial. *JAMA* **324**, 848–858 (2020).
4. Matthay, M. A. et al. Acute respiratory distress syndrome. *Nat. Rev. Dis. Prim.* **5**, 18 (2019).
5. Park, I. et al. Neutrophils disturb pulmonary microcirculation in sepsis-induced acute lung injury. *Eur. Respir. J.* **53**, 1800786 (2019).
6. Alsabani, M. et al. Reduction of NETosis by targeting CXCR1/2 reduces thrombosis, lung injury, and mortality in experimental human and murine sepsis. *Br. J. Anaesth.* **128**, 283–293 (2022).
7. Li, Z. et al. BMX represses thrombin-PAR1-mediated endothelial permeability and vascular leakage during early sepsis. *Circ. Res.* **126**, 471–485 (2020).
8. Sun, X. et al. Transcriptional switch of hepatocytes initiates macrophage recruitment and T-cell suppression in endotoxemia. *J. Hepatol.* **77**, 436–452 (2022).
9. Godoy-Tena, G. et al. Epigenetic and transcriptomic reprogramming in monocytes of severe COVID-19 patients reflects alterations in myeloid differentiation and the influence of inflammatory cytokines. *Genome Med.* **14**, 134 (2022).
10. Yuan, F. et al. Z-DNA binding protein 1 promotes heatstroke-induced cell death. *Science* **376**, 609–615 (2022).
11. Lei, Y. et al. Cooperative sensing of mitochondrial DNA by ZBP1 and cGAS promotes cardiotoxicity. *Cell* **186**, 3013–3032.e3022 (2023).
12. Jiao, H. et al. Z-nucleic-acid sensing triggers ZBP1-dependent necroptosis and inflammation. *Nature* **580**, 391–395 (2020).
13. Wu, Y. et al. Spatiotemporal immune landscape of colorectal cancer liver metastasis at single-cell level. *Cancer Discov.* **12**, 134–153 (2022).

14. Aibar, S. et al. SCENIC: single-cell regulatory network inference and clustering. *Nat. Methods* **14**, 1083–1086 (2017).
15. Bischoff, P. et al. Single-cell RNA sequencing reveals distinct tumor microenvironmental patterns in lung adenocarcinoma. *Oncogene* **40**, 6748–6758 (2021).
16. Street, K. et al. Slingshot: cell lineage and pseudotime inference for single-cell transcriptomics. *BMC Genomics* **19**, 477 (2018).
17. Gulati, G. S. et al. Single-cell transcriptional diversity is a hallmark of developmental potential. *Science* **367**, 405–411 (2020).
18. Pearce, E. L. & Pearce, E. J. Metabolic pathways in immune cell activation and quiescence. *Immunity* **38**, 633–643 (2013).
19. Cheng, S. C. et al. Broad defects in the energy metabolism of leukocytes underlie immunoparalysis in sepsis. *Nat. Immunol.* **17**, 406–413 (2016).
20. Shalova, I. N. et al. Human monocytes undergo functional re-programming during sepsis mediated by hypoxia-inducible factor-1α. *Immunity* **42**, 484–498 (2015).
21. Bill, R. et al. CXCL9:SPP1 macrophage polarity identifies a network of cellular programs that control human cancers. *Science* **381**, 515–524 (2023).
22. Hulsmans, M. et al. Recruited macrophages elicit atrial fibrillation. *Science* **381**, 231–239 (2023).
23. Yang, J. et al. Hemorrhagic shock primes for lung vascular endothelial cell pyroptosis: role in pulmonary inflammation following LPS. *Cell Death Dis.* **7**, e2363 (2016).
24. Xiang, M. et al. Hemorrhagic shock activates lung endothelial reduced nicotinamide adenine dinucleotide phosphate (NADPH) oxidase via neutrophil NADPH oxidase. *Am. J. Respir. Cell Mol. Biol.* **44**, 333–340 (2011).
25. de Reuver, R. et al. ADAR1 prevents autoinflammation by suppressing spontaneous ZBP1 activation. *Nature* **607**, 784–789 (2022).
26. Devos, M. et al. Sensing of endogenous nucleic acids by ZBP1 induces keratinocyte necroptosis and skin inflammation. *J. Exp. Med.* **217**, e20191913 (2020).
27. Schwarzer, R., Jiao, H., Wachsmuth, L., Tresch, A. & Pasparakis, M. FADD and caspase-8 regulate gut homeostasis and inflammation by controlling MLKL- and GSDMD-mediated death of intestinal epithelial cells. *Immunity* **52**, 978–993.e976 (2020).
28. Liu, L. et al. Proinflammatory signal suppresses proliferation and shifts macrophage metabolism from Myc-dependent to HIF1α-dependent. *Proc. Natl. Acad. Sci. USA* **113**, 1564–1569 (2016).
29. Owen, A. M. et al. Chronic muscle weakness and mitochondrial dysfunction in the absence of sustained atrophy in a preclinical sepsis model. *eLife* **8**, e49920 (2019).
30. West, A. P. et al. TLR signalling augments macrophage bactericidal activity through mitochondrial ROS. *Nature* **472**, 476–480 (2011).
31. Timblin, G. A. et al. Mitohormesis reprogrammes macrophage metabolism to enforce tolerance. *Nat. Metab.* **3**, 618–635 (2021).
32. Nargund, A. M., Fiorese, C. J., Pellegrino, M. W., Deng, P. & Haynes, C. M. Mitochondrial and nuclear accumulation of the transcription factor ATFS-1 promotes OXPHOS recovery during the UPR(mt). *Mol. Cell* **58**, 123–133 (2015).
33. Zhang, H. et al. Pre-operative exercise therapy triggers anti-inflammatory trained immunity of Kupffer cells through metabolic reprogramming. *Nat. Metab.* **3**, 843–858 (2021).
34. Blériot, C. et al. A subset of Kupffer cells regulates metabolism through the expression of CD36. *Immunity* **54**, 2101–2116.e2106 (2021).
35. Kim, J. W., Tchernyshyov, I., Semenza, G. L. & Dang, C. V. HIF-1-mediated expression of pyruvate dehydrogenase kinase: a metabolic switch required for cellular adaptation to hypoxia. *Cell Metab.* **3**, 177–185 (2006).
36. Palsson-McDermott, E. M. et al. Pyruvate kinase M2 regulates Hif-1α activity and IL-1β induction and is a critical determinant of the Warburg effect in LPS-activated macrophages. *Cell Metab.* **21**, 65–80 (2015).
37. Tannahill, G. M. et al. Succinate is an inflammatory signal that induces IL-1β through HIF-1α. *Nature* **496**, 238–242 (2013).
38. Nassour, J. et al. Telomere-to-mitochondria signalling by ZBP1 mediates replicative crisis. *Nature* **614**, 767–773 (2023).
39. Subramanian, N., Natarajan, K., Clatworthy, M. R., Wang, Z. & Germain, R. N. The adaptor MAVS promotes NLRP3 mitochondrial localization and inflammasome activation. *Cell* **153**, 348–361 (2013).
40. Kuriakose, T. et al. ZBP1/DAI is an innate sensor of influenza virus triggering the NLRP3 inflammasome and programmed cell death pathways. *Sci. Immunol.* **1**, aag2045 (2016).
41. Zheng, M., Karki, R., Vogel, P. & Kanneganti, T. D. Caspase-6 is a key regulator of innate immunity, inflammasome activation, and host defense. *Cell* **181**, 674–687.e613 (2020).
42. Lee, S. et al. AIM2 forms a complex with pyrin and ZBP1 to drive PANoptosis and host defence. *Nature* **597**, 415–419 (2021).
43. Ulland, T. K. et al. Nlrp12 mutation causes C57BL/6J strain-specific defect in neutrophil recruitment. *Nat. Commun.* **7**, 13180 (2016).
44. Hao, Y. et al. Integrated analysis of multimodal single-cell data. *Cell* **184**, 3573–3587.e3529 (2021).
45. Korsunsky, I. et al. Fast, sensitive and accurate integration of single-cell data with Harmony. *Nat. Methods* **16**, 1289–1296 (2019).
46. Yang, L. et al. Single-cell Mayo Map (scMayoMap): an easy-to-use tool for cell type annotation in single-cell RNA-sequencing data analysis. *BMC Biol.* **21**, 223 (2023).
47. Liu, B. et al. An entropy-based metric for assessing the purity of single cell populations. *Nat. Commun.* **11**, 3155 (2020).
48. Jin, S. et al. Inference and analysis of cell-cell communication using CellChat. *Nat. Commun.* **12**, 1088 (2021).

Acknowledgements

We thank Chaowei Shang, Ph.D., Director of Microscopy Facility at the University of Pittsburgh for assistance with confocal microscopy and immunofluorescence. This work was supported by the US National Institutes of Health Grant R01-HL-139547 (J.F.) and R21AI185275 (J.F.), US Department of Veterans Affairs Award 1I01BX004838 (J.F.) and IK6BX006297 (J.F.).

Author contributions

All authors contributed to the study conception and design. Material and animal preparation, data collection, and analysis were performed by T.G., Y.F., Q.W., Y.L., and P.A.L.; T.G., Z.W., T.R.B., Y.L., and J.F. planned the project and conceived the experiments. T.G., Y.L., and J.F. wrote the manuscript. All authors approved the final manuscript.

Competing interests

The authors declare no competing interests.

Additional information

Supplementary information The online version contains supplementary material available at https://doi.org/10.1038/s42003-024-07072-x.

Correspondence and requests for materials should be addressed to Ting Gong or Jie Fan.

Peer review information *Communications Biology* thanks the anonymous reviewers for their contribution to the peer review of this work. Primary handling editors: Connie Wong and Joao Valente.